Journal of Physics D:
Applied Physics



**PAPER** • **OPEN ACCESS**

# Structural and nanoacoustic characterization of Co/Pt ferromagnetic superlattices

To cite this article: E R Cardozo de Oliveira *et al* 2025 *J. Phys. D: Appl. Phys.* **58** 455301



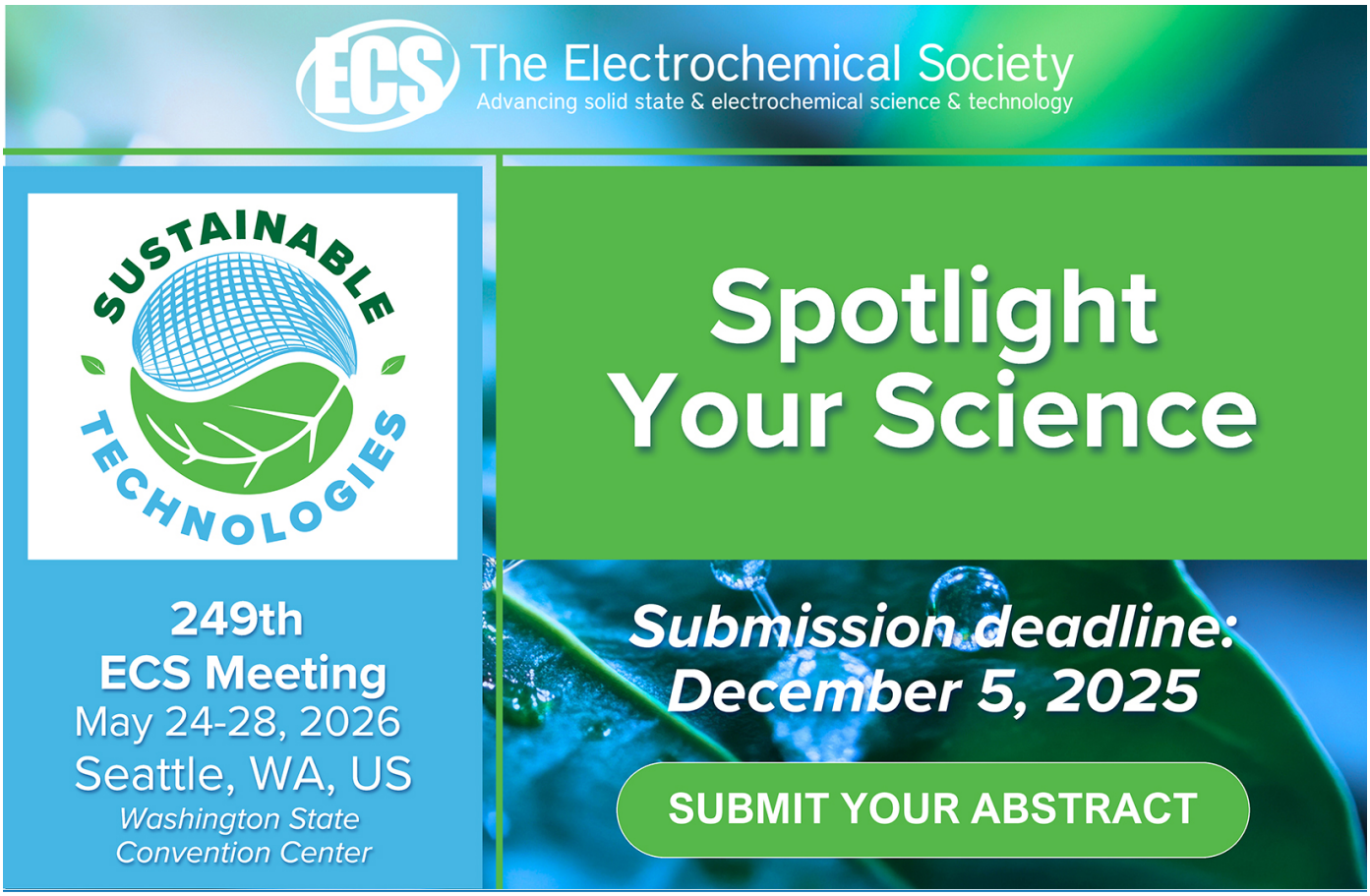

OPEN ACCESS
IOP Publishing
Journal of Physics D: Applied Physics
J. Phys. D: Appl. Phys. **58** (2025) 455301 (10pp)
https://doi.org/10.1088/1361-6463/ae148a

# Structural and nanoacoustic characterization of Co/Pt ferromagnetic superlattices

**E R Cardozo de Oliveira[1], C Xiang[1], C Borrazás[2], S Sandeep[1], J E Gómez[3], M Vasquez Mansilla[3], N Findling[1], L Largeau[1], N D Lanzillotti-Kimura[1] and M Granada[3,4,*]**

[1] Université Paris-Saclay, C.N.R.S., Centre de Nanosciences et de Nanotechnologies (C2N), 10 Boulevard Thomas Gobert, 91120 Palaiseau, France
[2] Universidad de Buenos Aires, Facultad de Ciencias Exactas y Naturales, Departamento de Física,1428 Buenos Aires, Argentina
[3] Instituto de Nanociencia y Nanotecnología CNEA-CONICET. Departamento de Magnetismo y Materiales Magnéticos, Gerencia de Física, Centro Atómico Bariloche, CNEA. Av. E. Bustillo 9500, R8402AGP San Carlos de Bariloche, Río Negro, Argentina
[4] Instituto Balseiro, Universidad Nacional de Cuyo-CNEA, Av. E. Bustillo 9500, San Carlos de Bariloche, Río Negro, R8402AGP, Argentina

E-mail: maragranada@cnea.gob.ar and daniel.kimura@cnrs.fr

Received 30 May 2025, revised 30 September 2025
Accepted for publication 17 October 2025
Published 3 November 2025

**Abstract**

Superlattices (SLs) with spatially modulated elastic properties-particularly those based on III–V semiconductors-have emerged as key platforms for reaching the ultrahigh-frequency (GHz–THz) regime in nanoacoustic devices. The exploration of alternative materials with multifunctional properties remains a rich and promising area of research. In this work, we investigate the structural, magnetic, and acoustic properties of nanometric Co/Pt SLs. X-ray reflectometry reveals a well-defined periodicity, while scanning transmission electron microscopy combined with local compositional analysis shows that the SLs exhibit a compositional modulation rather than sharp interfaces. The polycrystalline nature of the structures is confirmed by both x-ray diffraction and transmission electron microscopy. Magnetization measurements indicate the presence of perpendicular magnetic anisotropy at higher Co concentrations. Picosecond acoustic experiments demonstrate that the SLs support short-lived acoustic modes up to 900 GHz, along with up to seven acoustic echoes with frequencies ranging from 40 to 250 GHz. These findings open a path toward investigating phonon-driven magnetization dynamics in such structures, establishing a foundational step toward the development of magnetoacoustic devices operating at ultrahigh frequencies.

* Author to whom any correspondence should be addressed.

Keywords: nanoacoustic properties, ultrahigh-frequency phonons, ferromagnetic Co/Pt superlattices, nanometric metallic superlattices

## 1. Introduction

Ferromagnetic materials, such as Fe, Ni, Co, and their alloys, have long been foundational to data storage and processing technologies [1]. Magnetism in these materials is typically controlled by external magnetic fields, voltages, electric fields, or light [2–6]. Recently, acoustic phonons-the quanta of lattice vibrations-have gained attention as effective means for manipulating magnetism and spin dynamics through phonon–spin and phonon–magnon coupling. In the nanoacoustic regime, acoustic phonons with wavelengths on the nanoscale (ranging from 1 nm to 1 $\mu$m) correspond to frequencies in the GHz–THz range, where spin dynamics typically occur. Modifying their dispersion relation and density of states enhances their interactions with other excitations, presenting opportunities for compact, ultrafast devices, as well as applications in nanoscale material characterization, thermal transport, and quantum technologies [7–16].

Nanometer-scale superlattices (SLs) offer a versatile platform for tailoring the acoustic phonon dispersion. The additional periodicity introduced by the SLs reduces the Brillouin zone, folding the acoustic branches and creating acoustic minigaps at the zone edges and center [17–20]. The frequency and bandwidth of these gaps are governed by factors such as period thickness, composition, and relative layer thicknesses [21, 22]. As a result, acoustic SLs can serve as phonon filters, phonon mirrors in Fabry–Pérot resonators, or as building blocks for complex heterostructures designed to control both hypersound and light. For example, they have been used to emulate solid-state phenomena, including topological states, Bloch oscillations, and Anderson localization [21, 23–27].

Most phononic SLs reported to date are based on III–V semiconductors, although implementations have also been realized in oxides [28, 29], polymers [30, 31], and group-IV semiconductors [32–34], among others [35, 36]. This ongoing search for new material systems has driven the development of nanophononics toward novel functionalities, such as responsive devices with dynamically tunable acoustic responses under external control [37].

Metallic ferromagnetic multilayers, and particularly cobalt/platinum (Co/Pt) SLs, represent a promising platform for these applications. They exhibit perpendicular magnetic anisotropy (PMA), which can be tuned by adjusting the multilayer thickness and stacking sequence [38, 39]. This anisotropy is key for stabilizing magnetization perpendicular to the film plane-a property highly desirable for high-density spintronic applications. Additionally, Co/Pt SLs enable the engineering of acoustic phonon modes through periodic modulation of the elastic properties [40, 41]. While most previous studies have focused on confined GHz phonons in single metallic thin films, the ultrahigh-frequency (THz) acoustic phonon regime in magnetically ordered SLs remains largely unexplored [42].

In this work, we investigate the structural, magnetic, and nanoacoustic properties of ferromagnetic Co/Pt SLs. The central question we address is whether such systems can simultaneously sustain PMA and support ultrahigh-frequency acoustic modes, thus enabling a platform for ultrafast phonon–magnon interactions. We show that Co/Pt SLs host acoustic modes approaching 900 GHz and reveal acoustic echoes of phonons traversing the entire multilayer stack. These results position ferromagnetic SLs as a promising approach for dynamic control of magnetism at the nanoscale.

The article is organized as follows: section 2 describes the experimental methods. Section 3 presents the fabrication and structural/chemical characterization of the samples. Section 4 outlines the magnetic response, section 5 analyzes the coherent acoustic phonon dynamics, and section 6 discusses the implications and perspectives of our findings.

## 2. Methods

Co/Pt SLs were deposited by magnetron sputtering onto (001) Si substrates with a native oxide layer, under an argon pressure of $P_{\mathrm{Ar}} = 2.8$ mTorr, as described elsewhere [43]. The [Pt($t_{\mathrm{Pt}}$)/Co($t_{\mathrm{Co}}$)] bilayer was repeated 10 times, with a Pt($t_{\mathrm{Pt}}$) capping layer deposited on top. Here, $t_{\mathrm{Pt}}$ and $t_{\mathrm{Co}}$ represent the nominal thicknesses of the Pt and Co layers, respectively. The deposition time for Co (and thus $t_{\mathrm{Co}}$) was varied across the series of samples, while the deposition time for Pt was kept constant to achieve $t_{\mathrm{Pt}} = 4.2$ nm.

X-ray reflectometry (XRR) measurements were performed using a PANalytical XPert system equipped with a Cu anode in a sealed tube, with parallel plate collimators on both the incident and receiving paths. X-ray diffraction (XRD) measurements were carried out using a Rigaku Smartlab diffractometer, equipped with a rotating Cu anode and a five-circle goniometer. Non-coplanar grazing incidence x-ray diffraction (GIXRD) experiments were conducted with both the incident and collected beams nearly parallel to the sample surface, which allows for diffraction conditions of crystallographic planes perpendicular to the surface. This grazing incidence configuration enhances the diffraction from surface materials while maintaining a constant analysis direction in reciprocal space.

Scanning transmission electron microscopy (STEM) cross-section images were obtained with a FEI/ThermoFisher Themis Titan operating at 200 keV, equipped with a spherical aberration corrector for atomic resolution in STEM mode, and a Bruker Super-X detector for energy dispersive x-ray spectroscopy (EDS). The cross-section lamella was fabricated by focused ion beam (FIB) using a FEI/ThermoFisher dual-beam system.

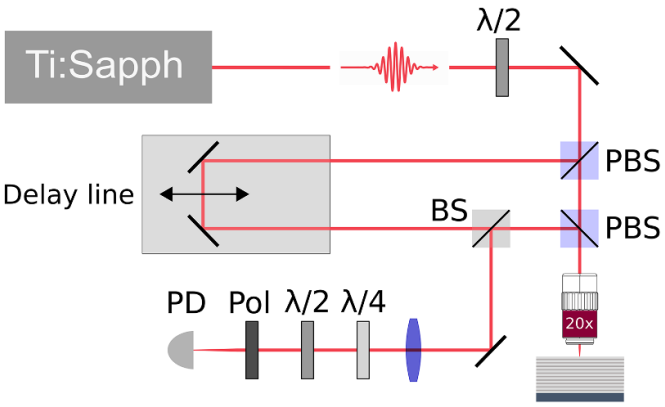


**Figure 1.** Schematics of the pump-probe experimental setup. BS, beam splitter; PBS, polarizing beam splitter; Pol, polarizer; $\lambda/2$, half-wave plate; $\lambda/4$, quarter-wave plate; PD, photodiode.

Magnetization loops were measured at room temperature using a custom-built magneto-optic Kerr effect (MOKE) magnetometer in the polar configuration, with the magnetic field applied normal to the sample plane. A red laser ($\lambda = 632$ nm, 5 mW) was incident on the sample surface, and the reflected beam passed through a nearly crossed polarizer, enabling sensitive detection of the Kerr rotation associated with the out-of-plane magnetization. The saturation magnetization was quantified using a Cryogenic S700X SQUID Magnetometer.

A pump-probe setup (see figure 1) was used to experimentally study the coherent acoustic phonon dynamics at room temperature [44, 45]. A Ti:sapphire laser generates $\sim 150$ fs pulses at a repetition rate of 80 MHz and a wavelength of 850 nm. A polarization beam splitter (PBS) divides the beam into two orthogonally polarized components: the pump and the probe, which follow different optical paths. Both beams are focused onto the sample using a 20X objective, resulting in a spot size of approximately 5 $\mu$m in diameter in a normal incidence configuration. The pump pulse first impinges on the sample, where it is absorbed, causing a rapid increase in electronic temperature that is subsequently transferred to the lattice, leading to thermalization. This ultrafast heating induces expansion, generating a strain pulse that propagates within the structure and produces folded acoustic phonons at the Brillouin zone center. The presence of these modes alters the complex refractive index in the multilayer, resulting in a variation of reflectivity ($\Delta R$) detected by the probe pulse, which arrives at the sample with a time delay. To enhance the signal-to-noise ratio, the pump beam is modulated at 800 kHz using an acousto-optical modulator, synchronized with a lock-in amplifier for synchronous detection. In the collection path, the pump beam is filtered out using a combination of half-wave and quarter-wave plates, along with a polarizer [46].

## 3. Structural characterization

XRR measurements were performed on all samples, revealing clear SL peaks along with the total thickness fringes (see figure 2(a)). For each set of peaks, the angular positions $\theta$ were indexed with integer numbers $m$. We then plotted $\sin^2\theta_m$ vs. $m^2$ and performed a linear fit. The modified Bragg law [47, 48], $\sin^2\theta_m = 2\delta + m^2(\lambda/2d)^2$, was used to obtain the interlayer distances $d$ from the slope of the linear fits, with $\lambda$ being the wavelength of Cu K$\alpha$ radiation. The SL period was extracted from the higher intensity peaks, while the total thickness of the sample was obtained from the smaller fringes. These parameters are listed in table 1 for all the samples. To estimate the individual Pt and Co layer thicknesses, which cannot be directly obtained from this analysis, we proceeded as follows. We plotted the XRR-derived thicknesses as a function of Co deposition time and performed a linear fit. This provided the Pt thickness as the ordinate (i.e. the thickness extrapolated to a Co deposition time of zero) and the Co deposition rate as the slope. For the period, a single layer of each material was considered, while the total thickness corresponds to 10 Co layers and 11 Pt layers. Both data sets yielded consistent values. Assuming pure Pt and Co layers, we obtained the average Pt thickness $t_{Pt} = (4.2 \pm 0.1)$ nm, and a Co deposition rate of $(1.8 \pm 0.6)$ nm min$^{-1}$, resulting in Co thicknesses $t_{Co}$ ranging from 0.18 to 0.72 nm across the series of SLs. The samples studied in this work are listed in table 1: SL18 ($t_{Co} = 0.18$ nm), SL45 ($t_{Co} = 0.45$ nm), SL54 ($t_{Co} = 0.54$ nm), and SL72 ($t_{Co} = 0.72$ nm).

**Table 1.** This table lists the nominal Co layer thickness $t_{Co}$, estimated from the deposition rate, and the total thickness and period obtained from XRR for each sample. The numbers in parentheses represent the error in the last digit. Saturation magnetization $M_S$, obtained by SQUID magnetometry at room temperature, is also presented.

| Sample | $t_{Co}$ (nm) | Total thickness (nm) | Period (nm) | $M_S$ (emu cm$^{-3}$) |
|---|---|---|---|---|
| SL18 | 0.18 | 48.94(9) | 4.45(5) | 82 |
| SL45 | 0.45 | 50.59(7) | 4.64(2) | 815 |
| SL54 | 0.54 | 52.88(8) | 4.81(4) | 905 |
| SL72 | 0.72 | 54.07(7) | 4.88(3) | 1003 |

Complementary XRD and transmission electron microscopy (TEM) with EDS were performed on the sample with the largest total thickness, SL72.

XRD patterns obtained in the conventional high-angle Bragg–Brentano configuration did not exhibit any clear peaks corresponding to the SL, with only intense peaks from the Si substrate observed. Non-coplanar GIXRD experiments were performed on sample SL72 to improve the observation of surface material. As described in section 2, the employed configuration allows diffraction from families of planes perpendicular to the surface. The sample was first aligned using the (220) and (440) substrate peaks (black curve in figure 2(b)). Due to the weak intensity of the collected signal, the monochromator was not used in this configuration, resulting in multiple wavelengths in the incident radiation (Cu K$\alpha$ and K$\beta$, W L$\alpha$). These wavelengths give rise to the diffraction peaks for silicon identified with asterisks in the figure. The remaining peaks, which have lower intensity and broader widths, are associated with the SL. To confirm this, the experiment was

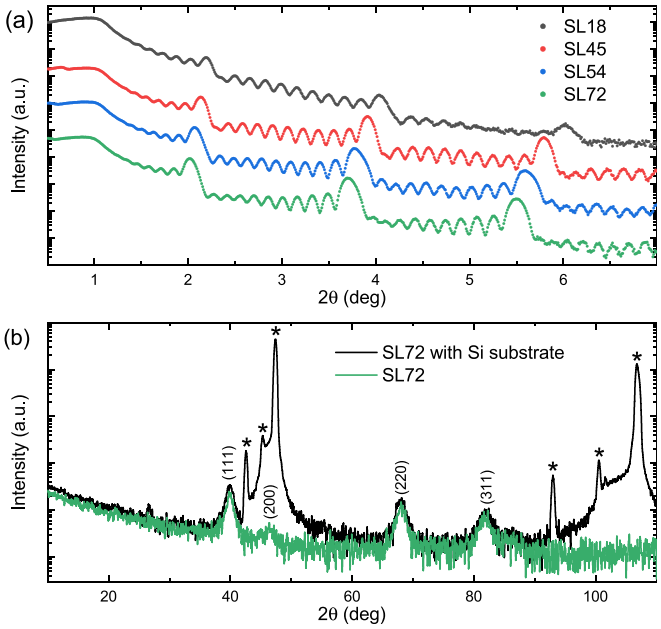


**Figure 2.** (a) XRR of the SLs $[Pt(t_{Pt})/Co(t_{Co})]_{10}/Pt(t_{Pt})$ studied in this work, measured with Cu K$\alpha$ radiation. The highest intensity peaks are associated with the SL period, while the lower intensity peaks with smaller separation are linked to the total thickness of the sample. (b) Non-coplanar GIXRD patterns. The black curve was obtained with the substrate in the Bragg condition, with the Si diffraction peaks (220) and (440) indicated (*). The multiplicity of those peaks is due to the presence of multiple wavelengths in the experiment, as discussed in the text. The green curve was obtained with the substrate out of the Bragg condition, confirming that the remaining peaks are associated with the SL. These peaks are labeled with the Miller indices of the conventional cubic unit cell for Pt.

repeated with the substrate out of the Bragg condition, yielding diffraction peaks consistent with the SL (green curve in figure 2(b)), which are labeled with Miller indices corresponding to the fcc structure. The intensity of these peaks is the same in both diffractograms, indicating the absence of a particular crystalline texture in the plane. Notably, the (200) orientation is almost absent, suggesting that this orientation is particularly unfavorable. From these peak positions, using the Cu K$\alpha$ radiation wavelength, we estimated the interplanar distances, which are listed in table 2. For comparison, the interplanar distances for Pt and Co in the fcc structure are also provided [49, 50]. Interestingly, the interplanar distances of the SL deviate from those of pure Pt by less than 1%, while those for Co are more than 10% smaller.

Figure 3(a) shows a STEM cross-section image of SL72. In the high-angle annular dark field (HAADF) mode, contrast is sensitive to atomic number, with heavier elements appearing brighter. The ten Pt/Co periods and the Pt capping layer are clearly visible. EDS analysis was used to quantify the atomic composition across the SL. The layers are continuous and homogeneous in both thickness and composition. Regions with higher roughness are observed, likely due to the presence of crystalline grains. High-resolution TEM images reveal

**Table 2.** Miller indices for the first Bragg reflections referring to the fcc structure with a cubic unit cell, and the interplanar distances $d_{SL}$ computed for the SL from the angular positions of the diffraction peaks in figure 2(b) using Cu K$\alpha$ radiation. The interplanar distances for Pt and Co, extracted from crystallographic tables for these materials with cubic structure ($Fm\bar{3}m$ space group), are also listed [49, 50].

| Bragg reflection | $d_{SL}$ (Å) | $d_{Pt}$ (Å) | $d_{Co}$ (Å) |
|---|---|---|---|
| (111) | 2.2618 | 2.2650 | 2.0467 |
| (200) | — | 1.9616 | 1.7723 |
| (220) | 1.3772 | 1.3873 | 1.2532 |
| (311) | 1.1768 | 1.1826 | 1.0688 |

a polycrystalline structure, with grains that may span multiple SL periods (see figure 3(b)). Figure 3(c) presents local EDS analysis performed by sweeping a line profile across the SL. Both Co and Pt atoms are present throughout the sample, with a composition modulation that reaches a maximum Pt concentration of 95 at.% in Pt-rich regions, and a minimum of 65 at.% in the very thin Co-rich layers. These results confirm that the SLs present a well-defined periodic structure, with interfaces characterized by a smooth contrast gradient rather than a sharp transition. It is important to note that the TEM lamella is several tens of nm thick, so the apparent gradients at the interface may arise from interfacial roughness within the depth of the lamella.

## 4. Magnetic properties

Figure 4 shows the normalized magnetization loops measured by MOKE magnetometry in polar configuration at room temperature for those SLs exhibiting a perpendicular magnetic component. Square-shaped loops were obtained for samples with $t_{Co} \geqslant 0.45$ nm, indicating the presence of strong PMA. The coercive field $H_C$ is observed to increase with increasing Co thickness, consistent with previous reports on Pt/Co/Pt stacks [43, 48], and suggesting an enhancement of PMA with $t_{Co}$. In contrast, the sample with $t_{Co} = 0.18$ nm exhibited no detectable magnetic signal in this experiment, indicating the absence of a robust ferromagnetic response at this low Co thickness.

The saturation magnetization $M_S$ was determined from full magnetization loops obtained by SQUID magnetometry at room temperature for all samples. These values are listed in table 1. $M_S$ was calculated as the ratio between the saturation magnetic moment and the nominal volume of Co in each sample, estimated as the sample area multiplied by the nominal Co thickness $t_{Co}$. However, as evidenced by STEM characterization, this volume does not correspond to a pure Co phase, but rather to an intermixed Co–Pt region. Therefore, the measured values of $M_S$ should be interpreted as effective saturation magnetizations of a Co–Pt alloy, whose composition varies across the series. This intermixing explains the systematically lower $M_S$ values compared to bulk Co ($M_S = 1420$ emu cm$^{-3}$

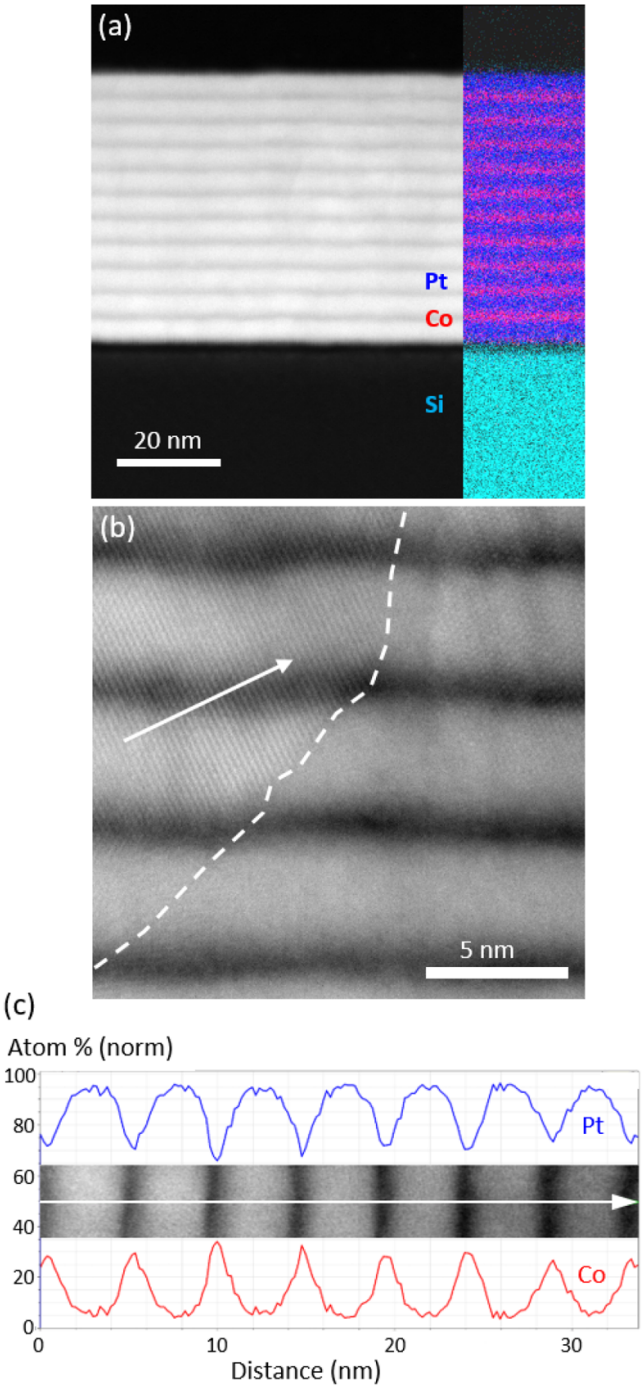


**Figure 3.** (a) Cross-sectional STEM image of SL72 obtained in the HAADF mode; on the right, the composition map indicates the presence of Si (substrate), Pt, and Co, detected by EDS analysis. (b) High-resolution HAADF-STEM image showing crystalline grains with different orientations. One grain, indicated by the dashed line, spans several SL periods. The planes perpendicular to the arrow are consistent with the (111) orientation. (c) Spatial distribution of Pt and Co atoms across the SL, determined by local EDS analysis restricted to these two atomic species; the scan-line is shown in the inset.

for hcp Co), while still being consistent with literature values reported for Co–Pt alloys with Pt atomic concentrations between 20% and 80% [51].

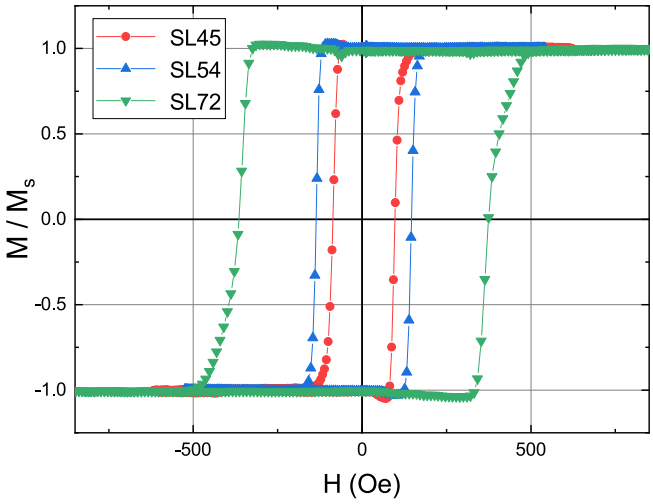


**Figure 4.** Normalized out-of-plane magnetization loops measured by MOKE magnetometry in polar configuration for SLs with different Co thicknesses. Square loops are observed in samples with $t_{Co} \geqslant 0.45$ nm at room temperature.

## 5. Ultrahigh-frequency acoustic phonon dynamics

Figure 5(a) shows the transient reflectivity signals measured for the four SLs. A sharp change in $\Delta R$ at $t = 0$ ps originates from ultrafast hot-electron dynamics during pump excitation. This is followed by a slower thermal relaxation of the system back to equilibrium. Superimposed on this relaxation, two distinct fast dynamics are observed: (1) short-period oscillations that decay within the first 7 ps, attributed to folded acoustic phonons arising from the SL periodicity, and (2) long-period oscillations that persist throughout the entire measurement window. The latter are associated with acoustic echoes of a strain pulse that propagates into the structure, reflects at the interface with the Si substrate, and returns to the surface, where it is detected again by the probe pulse. The attenuation of the acoustic signal is primarily due to phonon absorption in the materials and phonon scattering at the interfaces. Although phonon leakage into the substrate is often considered a loss mechanism, in this case, the large acoustic impedance mismatch between the metallic SL and the Si substrate significantly suppresses such leakage. To analyze the high- and low-frequency components of the signal, the raw data are separated into two time windows: 0–7 ps (figure 5(b)) and 10–200 ps (figure 5(c)).

In the 10–200 ps range, a polynomial fit is applied to remove the slow relaxation component, revealing oscillations with a period of approximately 25 ps and a decaying amplitude. A double-feature structure is also observed in figure 5(c). This behavior is likely related to phase relationships among higher-order harmonic contributions; however, its exact origin remains unclear and may involve multiple factors. Further investigation is required to clarify its nature. By performing a fast Fourier transform (FFT), the phononic spectra shown in figure 5(d) are obtained. A peak at ∼40 GHz is observed, corresponding to the fundamental mode of the

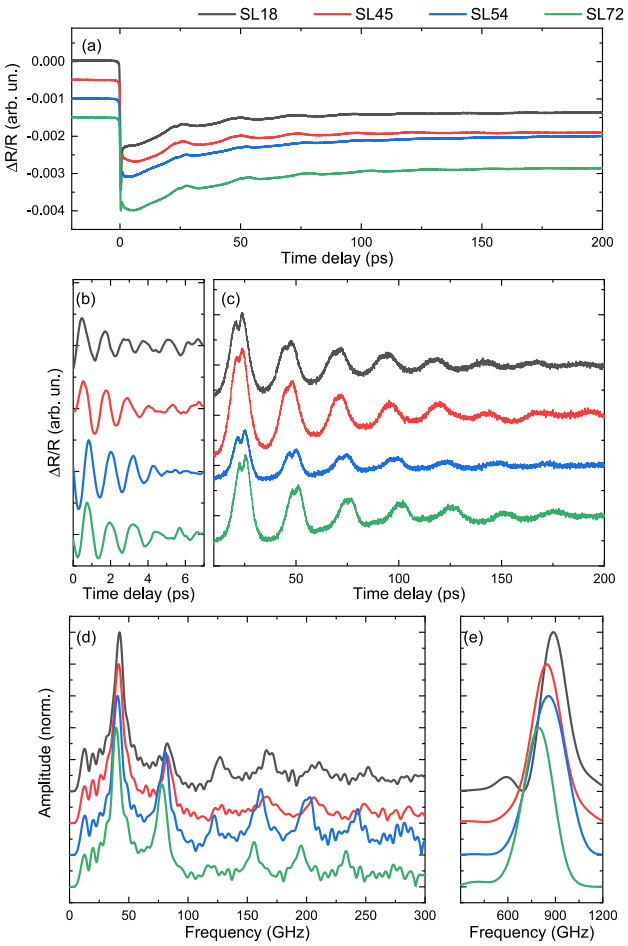


**Figure 5.** (a) Raw timetraces of SL18 (black), SL45 (red), SL54 (blue), and SL72 (green). (b) Band-pass filtered signals between 500 and 1500 GHz for the first 7 ps from traces shown in (a). (c) Polynomial fit applied to the 10–200 ps region. (d) FFT of the traces in (c). (e) FFT of the traces in (b).

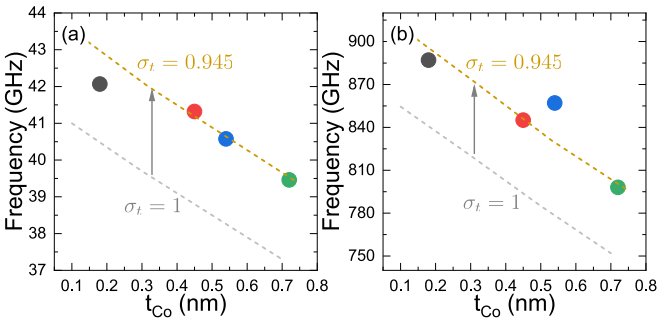


**Figure 6.** Peak positions of the modes at (a) ∼40 GHz and (b) ∼800 GHz for all superlattices. The dashed gray and dark yellow lines indicate theoretical frequencies obtained using different correction factors $\sigma_t$ applied to the nominal Pt and Co thicknesses in the transfer matrix simulations.

entire multilayer stack, considered as an effective single resonator. Additional harmonic peaks up to 250 GHz are also present.

For the 0–7 ps interval, the short-period oscillations are isolated by applying a band-pass filter between 500 and 1500 GHz on the raw signal (figure 5(b)). The corresponding FFT, shown in figure 5(e), reveals a high-frequency component at approximately 800 GHz.

The peak positions in the phononic spectra are extracted for all four samples. As the nominal Co layer thickness increases from 0.18 to 0.72 nm, the total sample thickness also increases, resulting in a redshift of the mode at 40 GHz, as shown in figure 6(a). Similarly, the unit cell thickness increases, producing a redshift of the mode at 800 GHz, as displayed in figure 6(b).

Frequency- and time-domain simulations of the acoustic properties of SL72 were performed using both the transfer matrix method, incorporating the photoelastic model, and the finite element method implemented in COMSOL [52, 53]. Figure 7(a) shows the acoustic dispersion relation for the longitudinal mode of SL72 within the first Brillouin zone. Two stop-band regions are clearly visible: one near ∼420 GHz at the zone edge and another at ∼850 GHz at the zone center. The amplitude and position of these stop-bands depend on material properties (sound velocity and mass density) and the SL period.

Using the transfer matrix method, we calculate the pump-probe generation-detection spectrum, shown in figure 7(b). Details of the simulation procedure are provided in [52], and the parameters used are listed in table 3. The resulting spectrum exhibits distinct features in two frequency ranges: between 40 and 300 GHz, and above 700 GHz. The lower-frequency peaks correspond to acoustic modes governed by the total thickness of the SL, which behaves as an acoustic resonator with a fundamental frequency near 40 GHz. Figures 7(c) and (d) show the displacement profiles of the fundamental mode (39.28 GHz) and its first harmonic (78.55 GHz), corresponding to the first and second peaks in figure 7(b). In both cases, the displacement profiles are commensurate with the full thickness of the SL.

In contrast, the higher-frequency peaks are associated with the lower and upper band-edge SL modes at the Brillouin zone center. The displacement profiles of these modes are shown in figures 7(e) and (f), where the periodicity is commensurate with both the SL period and the overall thickness.

We also simulated the dependence of the fundamental and SL mode frequencies on the cobalt thickness $t_{Co}$. The results, shown as dashed lines in figures 6(a) and (b), respectively, are compared to experimental data. To improve the agreement, a correction factor $\sigma_t$ was applied to the nominal Co and Pt thicknesses. Using nominal values ($\sigma_t = 1$) results in a deviation of ∼5.5% from the experimental data. Applying a correction factor of $\sigma_t = 0.945$ significantly improves the match across both frequency ranges.

These discrepancies may arise from several sources, including deviations in sound velocities for thin films, interdiffusion of Pt and Co atoms, and interface roughness-all of which are not included in the simulations but are present in the fabricated structures, as discussed in section 3. Despite these limitations, the strong agreement validates the simulation methodology and confirms its reliability in capturing the essential acoustic properties of the system.

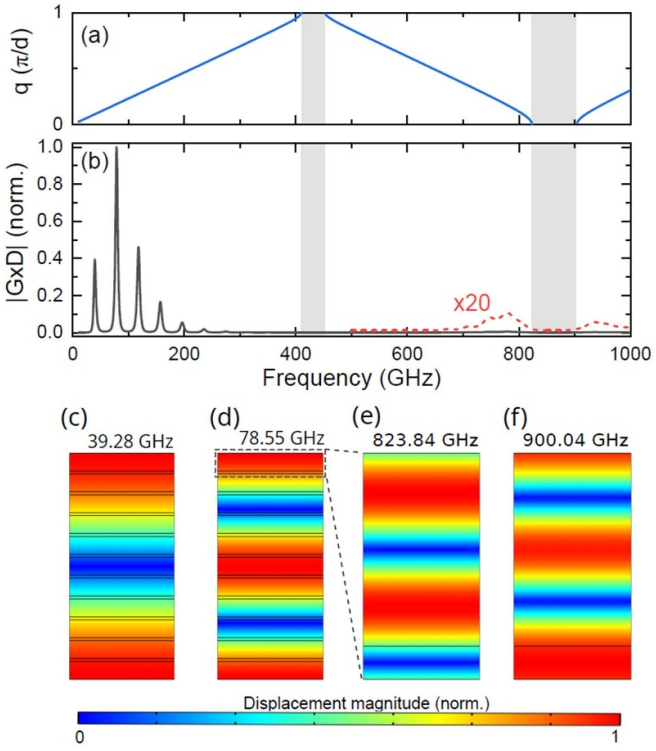


**Figure 7.** (a) Calculated acoustic dispersion relation of SL72. The stop-bands at ∼420 and ∼850 GHz are highlighted in gray. (b) Simulated pump-probe generation-detection spectrum. The lower-frequency modes correspond to the full stack, while the higher-frequency modes near 800 GHz correspond to superlattice modes. The red dashed line is scaled by a factor of 20 for clarity. (c) and (d) Displacement profiles across the full stack for the fundamental mode at ∼39 GHz and its first harmonic at ∼79 GHz, respectively. (e) and (f) Displacement profiles of superlattice modes at ∼800 GHz, shown over a single period. The black lines in (c)–(f) outline the different layers in the SL, and the vertical direction of these figures corresponds to depth of the superlattice.

**Table 3.** Parameters used in the simulations. $n$, $v$, $\rho$, and $\delta$ refer to refractive index, sound velocity, mass density, and optical penetration depth, respectively. The longitudinal sound velocities of Pt and Co were calculated using the Young's modulus ($E$), Poisson's ratio ($\nu$), and mass density ($\rho$), based on COMSOL's materials database and [54], via the relation $v = \sqrt{\frac{E(1-\nu)}{\rho(1+\nu)(1-2\nu)}}$.

| Material | $n$ | $v$ (m s$^{-1}$) | $\rho$ (g cm$^{-3}$) | $\delta$ (nm) |
|---|---|---|---|---|
| Pt | 3.01 + 5.19i [55, 56] | 3829.06 | 21.45 | 150 |
| Co | 2.57 + 4.99i [56, 57] | 5857.55 | 8.8 | 150 |
| Si [58] | 3.72 | 8433 | 2.32 | inf |

Time-domain simulations were carried out using two complementary approaches. In the first, an initial strain field containing spectral components from the generation spectrum-calculated over the 0–1000 GHz frequency range-is constructed. By applying an inverse Fourier transform, the temporal evolution of the strain field throughout the structure is obtained. From this, the initial optical reflectivity $r_0$ and

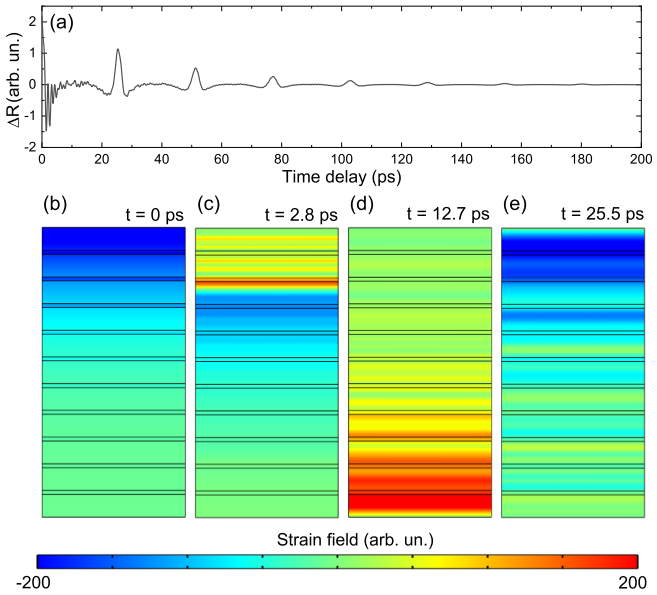


**Figure 8.** (a) Simulated timetrace using the transfer matrix method. (b)–(e) Strain field across the structure at (b) $t = 0$ ps, (c) $t = 2.8$ ps, (d) $t = 12.7$ ps, and (e) $t = 25.5$ ps, simulated with COMSOL. The black lines in (b)–(e) outline the different layers in the SL, and the vertical direction of these figures corresponds to depth of the superlattice.

the perturbed reflectivity $r'$ are calculated. For simplicity, reflectivity is computed at a single wavelength, $\lambda = 850$ nm, corresponding to the central wavelength of the laser used in both pump and probe beams. The initial reflectivity $r_0$ represents the response of the unperturbed (strain-free) structure. To compute $r'$, the strain field at each time step is used to modify the refractive index profile of the structure, modeled as $n' = n_0 + \Delta n$, with $\Delta n \propto \frac{\text{strain}}{n_0}$. The reflectivity change is then evaluated as $\Delta R = |r_0|^2 - |r'|^2$. The simulation was performed up to 200 ps, and the result is shown in figure 8(a). Notably, the simulation captures key features observed in the experimental time traces (figures 5(a)–(c)), including the rapid decay of high-frequency oscillations at early times and the periodic modulations occurring approximately every 25 ps.

In the second approach, implemented using COMSOL, the simulation begins with an initial strain field that peaks at the surface and decays gradually into the structure, emulating the optical skin depth. This depth is estimated by simulating the electric field distribution of the laser, based on the complex refractive indices of Pt and Co listed in table 3. The subsequent time evolution of the strain field is computed. Figures 8(b)–(e) show the strain field across the structure at selected time steps: (b) $t = 0$ ps, (c) $t = 2.8$ ps, (d) $t = 12.7$ ps, and (e) $t = 25.5$ ps. Panel 8(c) illustrates the propagation of the strain wave through the SL, revealing signatures of SL acoustic modes. In panel 8(d), the strain front reaches the bottom of the structure. Finally, in panel 8(e), the reflected acoustic wave returns to the surface, where detection efficiency is highest. This

round-trip propagation gives rise to the periodic modulations observed in both the experimental and simulated time-domain signals.

## 6. Conclusion and perspectives

In summary, we have investigated the structural, magnetic, and acoustic properties of four Pt/Co-based ferromagnetic SLs with varying cobalt thicknesses. XRR and STEM imaging confirmed the formation of sub-5 nm-thick periodic Pt–Co layers. The SLs exhibit clear out-of-plane magnetization hysteresis, with properties strongly dependent on Co content.

We demonstrated the generation and detection of ultrahigh-frequency acoustic phonons approaching 900 GHz, along with complex phonon dynamics below 300 GHz. Simulations using both the transfer matrix method and finite element modeling were performed to characterize the acoustic modes and their dynamics, supporting the experimental observations. Despite the simplified model assuming ideal Pt/Co stacking with sharp interfaces and nominal layer thicknesses from XRR, the simulations capture the main features of the measured phononic response. The dependence of phonon modes on Co thickness (and thus on SL period) highlights the capability of these systems for nanoscale phonon engineering, meeting key requirements of nanophononic applications.

Acoustic losses in Co/Pt SLs, primarily due to intrinsic absorption and phonon scattering at interfaces, remain a limitation for extending oscillation lifetimes. However, coherent phonons are still sustained up to ∼800 GHz, indicating that coherence is preserved when phonon wavelengths exceed the characteristic interface roughness. Improvements in deposition techniques to enhance interface sharpness could further increase phonon lifetimes. Moreover, exploring laser polarization as an additional control parameter may offer new possibilities for tailoring phonon generation and propagation in ferromagnetic SLs [59]. These nanoacoustic systems also show potential for integration with optical fiber platforms, providing improved stability and reproducibility in future experiments [46]. Given the strong spin–orbit coupling at Co/Pt interfaces, future studies should address the role of Dzyaloshinskii–Moriya interactions, chiral spin textures, and magnon damping in such systems. These effects, though beyond the scope of the present work, may significantly influence the magnetoacoustic coupling and offer additional pathways for phonon–magnon control at the nanoscale.

Despite current limitations, our results represent a step forward in the integration of ultrahigh-frequency acoustic phonons and magnons for magnophononic or magnonanomechanical applications, and demonstrate the potential of nanoscale SLs for controlling magnetic properties through acoustic fields.

## Data availability statement

All data that support the findings of this study are included within the article (and any supplementary files).

## Acknowledgments

The authors acknowledge support from the C N R S International Research Project Phenomenas. E R C de O , C X , S S , and N D L-K acknowledge funding from European Research Council Consolidator Grant No. 101045089 (T-Recs). M G and J E G acknowledge support from MSCA-RISE-H2020 ULTIMATE-I-Project No. 101007825 funded by the European Union. The authors acknowledge the French RENATECH network which partly funds the XRD characterizations, FIB preparation and TEM observations carried out in this work. We thank H Saraceni and F Napolitano (Dept. of Materials Characterization, Centro Atómico Bariloche, CNEA) for their assistance in the XRR measurements.

## ORCID iDs

E R Cardozo de Oliveira 0000-0002-5841-7832
C Xiang 0000-0002-8879-9966
C Borrazás 0009-0000-8740-8559
S Sandeep 0000-0002-1691-6342
J E Gómez 0000-0002-8408-9748
M Vasquez Mansilla 0000-0002-3829-7722
N Findling 0009-0002-9485-2521
L Largeau 0009-0003-0251-7273
N D Lanzillotti-Kimura 0000-0002-6056-5551
M Granada 0000-0003-0757-654X

## References

[1] Comstock R L 2002 Review modern magnetic materials in data storage *J. Mater. Sci. Mater. Electron.* **13** 509–23
[2] Beaurepaire E, Merle J-C, Daunois A and Bigot J-Y 1996 Ultrafast spin dynamics in ferromagnetic nickel *Phys. Rev. Lett.* **76** 4250–3
[3] Bigot J-Y, Guidoni L, Beaurepaire E and Saeta P N 2004 Femtosecond spectrotemporal magneto-optics *Phys. Rev. Lett.* **93** 077401
[4] Weisheit M, Fähler S, Marty A, Souche Y, Poinsignon C and Givord D 2007 Electric field-induced modification of magnetism in thin-film ferromagnets *Science* **315** 349–51
[5] Chu Y-H *et al* 2008 Electric-field control of local ferromagnetism using a magnetoelectric multiferroic *Nat. Mater.* **7** 478–82
[6] Rana B and Otani Y 2019 Towards magnonic devices based on voltage-controlled magnetic anisotropy *Commun. Phys.* **2** 1–12
[7] Kittel C 1958 Interaction of spin waves and ultrasonic waves in ferromagnetic crystals *Phys. Rev.* **110** 836–41
[8] Li Y, Zhao C, Zhang W, Hoffmann A and Novosad V 2021 Advances in coherent coupling between magnons and acoustic phonons *APL Mater.* **9** 060902
[9] Yang W-G and Schmidt H 2021 Acoustic control of magnetism toward energy-efficient applications *Appl. Phys. Rev.* **8** 021304
[10] Hioki T, Hashimoto Y and Saitoh E 2022 Coherent oscillation between phonons and magnons *Commun. Phys.* **5** 1–8
[11] Weber M C *et al* 2022 Emerging spin–phonon coupling through cross-talk of two magnetic sublattices *Nat. Commun.* **13** 443
[12] Kalashnikova A M, Kimel A V, Pisarev R V, Gridnev V N, Kirilyuk A and Rasing T 2007 Impulsive generation of

coherent magnons by linearly polarized light in the easy-plane antiferromagnet $FeBO_3$ *Phys. Rev. Lett.* **99** 167205
[13] Scherbakov A V, Salasyuk A S, Akimov A V, Liu X, Bombeck M, Brüggemann C, Yakovlev D R, Sapega V F, Furdyna J K and Bayer M 2010 Coherent magnetization precession in ferromagnetic (Ga,Mn)As induced by picosecond acoustic pulses *Phys. Rev. Lett.* **105** 117204
[14] Thevenard L, Peronne E, Gourdon C, Testelin C, Cubukcu M, Charron E, Vincent S, Lemaitre A and Perrin B 2010 Effect of picosecond strain pulses on thin layers of the ferromagnetic semiconductor (Ga, Mn)(As, P) *Phys. Rev. B* **82** 104422
[15] Kuszewski P, Duquesne J-Y, Becerra L, Lemaitre A, Vincent S, Majrab S, Margaillan F, Gourdon C and Thevenard L 2018 Optical probing of Rayleigh wave driven magnetoacoustic resonance *Phys. Rev. Appl.* **10** 034036
[16] Thevenard L, Camara I S, Majrab S, Bernard M, Rovillain P, Lemaitre A, Gourdon C and Duquesne J-Y 2016 Precessional magnetization switching by a surface acoustic wave *Phys. Rev. B* **93** 134430
[17] Huynh A, Perrin B and Lemaitre A 2015 Semiconductor superlattices: a tool for terahertz acoustics *Ultrasonics* **56** 66–79
[18] Lanzillotti-Kimura N D, Fainstein A, Lemaitre A and Jusserand B 2006 Nanowave devices for terahertz acoustic phonons *Appl. Phys. Lett.* **88** 083113
[19] Lanzillotti-Kimura N D, Fainstein A, Jusserand B, Lemaitre A, Mauguin O and Largeau L 2007 Acoustic phonon nanowave devices based on aperiodic multilayers: experiments and theory *Phys. Rev. B* **76** 174301
[20] Narayanamurti V, Störmer H L, Chin M A, Gossard A C and Wiegmann W 1979 Selective transmission of high-frequency phonons by a superlattice: the 'dielectric' phonon filter *Phys. Rev. Lett.* **43** 2012–6
[21] Ortiz O, Priya P, Rodriguez A, Lemaitre A, Esmann M and Lanzillotti-Kimura N D 2021 Topological optical and phononic interface mode by simultaneous band inversion *Optica* **8** 598
[22] Ortíz O, Esmann M and Lanzillotti-Kimura N D 2019 Phonon engineering with superlattices: generalized nanomechanical potentials *Phys. Rev. B* **100** 085430
[23] Arregui G , Ortíz O, Esmann M, Sotomayor-Torres C M, Gomez-Carbonell C, Mauguin O, Perrin B, Lemaitre A, García P D and Lanzillotti-Kimura N D 2019 Coherent generation and detection of acoustic phonons in topological nanocavities *APL Photonics* **4** 030805
[24] Esmann M, Lamberti F R, Senellart P, Favero I, Krebs O, Lanco L, Gomez Carbonell C, Lemaitre A and Lanzillotti-Kimura N D 2018 Topological nanophononic states by band inversion *Phys. Rev. B* **97** 155422
[25] Rodriguez A, Papatryfonos K, Cardozo De Oliveira E R and Lanzillotti-Kimura N D 2023 Topological nanophononic interface states using high-order bandgaps in the one-dimensional Su-Schrieffer-Heeger model *Phys. Rev. B* **108** 205301
[26] Lanzillotti-Kimura N D, Fainstein A, Perrin B, Jusserand B, Mauguin O, Largeau L and Lemaitre A 2010 Bloch oscillations of THz acoustic phonons in coupled nanocavity structures *Phys. Rev. Lett.* **104** 197402
[27] Arregui G, Lanzillotti-Kimura N D, Sotomayor-Torres C M and García P D 2019 Anderson photon-phonon colocalization in certain random superlattices *Phys. Rev. Lett.* **122** 043903
[28] Lanzillotti-Kimura N D, Fainstein A, Perrin B, Jusserand B, Soukiassian A, Xi X X and Schlom D G 2010 Enhancement and inhibition of coherent phonon emission of a Ni film in a $BaTiO_3$ /$SrTiO_3$ cavity *Phys. Rev. Lett.* **104** 187402
[29] Bruchhausen A E, Lanzillotti-Kimura N D, Jusserand B, Soukiassian A, Xie L, Pan X Q, Dekorsy T, Schlom D G and Fainstein A 2018 Acoustic confinement phenomena in oxide multifunctional nanophononic devices *Phys. Rev. Mater.* **2** 106002
[30] Gomopoulos N, Maschke D, Koh C Y, Thomas E L, Tremel W, Butt H-J and Fytas G 2010 One-dimensional hypersonic phononic crystals *Nano Lett.* **10** 980–4
[31] Schneider D, Liaqat F, El Boudouti E H, El Abouti O, Tremel W, Butt H-J, Djafari-Rouhani B and Fytas G 2013 Defect-controlled hypersound propagation in hybrid superlattices *Phys. Rev. Lett.* **111** 164301
[32] Ezzahri Y, Grauby S, Rampnoux J M, Michel H, Pernot G, Claeys W, Dilhaire S, Rossignol C, Zeng G and Shakouri A 2007 Coherent phonons in Si/SiGe superlattices *Phys. Rev. B* **75** 195309
[33] Wilson T E 2018 Evidence for terahertz acoustic phonon parametric oscillator based on acousto-optic degenerate four-wave mixing in a silicon doping superlattice *Phys. Rev. B* **98** 220304
[34] Parsons L C and Andrews G T 2012 Brillouin scattering from porous silicon-based optical Bragg mirrors *J. Appl. Phys.* **111** 123521
[35] Perrin B, Bonello B, Jeannet J-C and Romatet E 1996 Picosecond ultrasonics study of metallic multilayers *Physica B* **219–220** 681–3
[36] Cardozo De Oliveira E R, Vensaus P, Soler-Illia G J A A and Lanzillotti-Kimura N D 2023 Design of cost-effective environment-responsive nanoacoustic devices based on mesoporous thin films *Opt. Mater. Express* **13** 3715
[37] Priya P, Cardozo de Oliveira E R and Lanzillotti-Kimura N D 2023 Perspectives on high-frequency nanomechanics, nanoacoustics and nanophononics *Appl. Phys. Lett.* **122** 140501
[38] Hashimoto S and Ochiai Y 1990 Co/Pt and Co/Pd multilayers as magneto-optical recording materials *J. Magn. Magn. Mater.* **88** 211–26
[39] Hashimoto S, Ochiai Y and Aso K 1990 Film thickness dependence of magneto-optical and magnetic properties in Co/Pt and Co/Pd multilayers *J. Appl. Phys.* **67** 4429–31
[40] Shim J-H, Ali Syed A, Kim C-H, Lee K M, Park S-Y, Jeong J-R, Kim D-H and Eon Kim D 2017 Ultrafast giant magnetic cooling effect in ferromagnetic Co/Pt multilayers *Nat. Commun.* **8** 796
[41] Kim C H, Shim J-H, Lee K M, Jeong J-R, Kim D-H and Kim D E 2016 Coherent phonon control via electron-lattice interaction in ferromagnetic Co/Pt multilayers *Sci. Rep.* **6** 1–8
[42] Gu R *et al* 2024 Superorders and terahertz acoustic modes in multiferroic $BiFeO_3$/$LaFeO_3$ superlattices *Appl. Phys. Rev.* **11** 041415
[43] Quinteros C P, Bustingorry S, Curiale J and Granada M 2018 Correlation between domain wall creep parameters of thin ferromagnetic films *Appl. Phys. Lett.* **112** 262402
[44] Rossignol C and Perrin B 2001 Picosecond ultrasonics study of periodic multilayers *Anal. Sci./Supplements* **17** s245–8
[45] Thomsen C, Grahn H T, Maris H J and Tauc J 1986 Surface generation and detection of phonons by picosecond light pulses *Phys. Rev. B* **34** 4129–38
[46] Ortiz O *et al* 2020 Fiber-integrated microcavities for efficient generation of coherent acoustic phonons *Appl. Phys. Lett.* **117** 183102
[47] Nakamura O, Fullerton E E, Guimpel J and Schuller I K 1992 High $T_C$ thin films with roughness smaller than one unit cell *Appl. Phys. Lett.* **64** 120
[48] Quinteros C P, Cortés Burgos M J, Albornoz L J, Gómez J E, Granell P, Golmar F, Ibarra M L, Bustingorry S, Curiale J and Granada M 2021 Impact of growth conditions on the

domain nucleation and domain wall propagation in Pt/Co/Pt stacks *J. Phys. D: Appl. Phys.* **54** 015002
[49] Pt crystallographic ref:pdf-2 ICDD file 00-004-0802 (available at: www.icdd.com/pdfsearch/)
[50] Co crystallographic ref:pdf-2 ICDD file 00-015-0806 (available at: www.icdd.com/pdfsearch/)
[51] Nozawa N, Saito S, Hinata S and Takahashi M 2013 Large uniaxial magnetocrystalline anisotropy for $Co_{50}Pt_{50}$ disordered alloy films with hexagonal-close-packed stacking structure by substituting Pt with Rh *J. Phys. D: Appl. Phys.* **46** 172001
[52] Lanzillotti-Kimura N D, Fainstein A, Perrin B and Jusserand B 2011 Theory of coherent generation and detection of THz acoustic phonons using optical microcavities *Phys. Rev. B* **84** 064307
[53] Pascual-Winter M F, Fainstein A, Jusserand B, Perrin B and Lemaitre A 2012 Spectral responses of phonon optical generation and detection in superlattices *Phys. Rev. B* **85** 235443
[54] Matweb, material property data, Cobalt, (available at: www.matweb.com/search/-datasheet.aspx?bassnum = AMECo00)
[55] Rakić A D, Djurišić A B, Elazar J M and Majewski M L 1998 Optical properties of metallic films for vertical-cavity optoelectronic devices *Appl. Opt.* **37** 5271
[56] Polyanskiy M N 2024 Refractiveindex.info database of optical constants *Sci. Data* **11** 94
[57] Johnson P and Christy R 1974 Optical constants of transition metals: Ti, V, Cr, Mn, Fe, Co, Ni and Pd *Phys. Rev. B* **9** 5056–70
[58] Cardozo de Oliveira E R, Xiang C, Esmann M, Lopez Abdala N, Fuertes M C, Bruchhausen A, Pastoriza H, Perrin B, Soler-Illia G J A A and Lanzillotti-Kimura N D 2023 Probing gigahertz coherent acoustic phonons in $TiO_2$ mesoporous thin films *Photoacoustics* **30** 100472
[59] Lanzillotti-Kimura N D, O'Brien K P, Rho J, Suchowski H, Yin X and Zhang X 2018 Polarization-controlled coherent phonon generation in acoustoplasmonic metasurfaces *Phys. Rev. B* **97** 235403